HOKKAIDO UNIVERSITY

Title	Surface chemistry and radionuclide anion immobilisation potential of phosphoric acid-activated metakaolin-based geopolymers
Author(s)	Niu, Xiaobo; Elakneswaran, Yogarajah; Hiroyoshi, Naoki
Citation	Cement and Concrete Research, 181, 107549 https://doi.org/10.1016/j.cemconres.2024.107549
Issue Date	2024-07
Doc URL	https://hdl.handle.net/2115/97252
Rights	© <2024>. This manuscript version is made available under the CC-BY-NC-ND 4.0 license https://creativecommons.org/licenses/by-nc-nd/4.0/
Rights(URL)	https://creativecommons.org/licenses/by-nc-nd/4.0/
Type	journal article
File Information	PBG Manuscript.pdf

Hokkaido University Collection of Scholarly and Academic Papers : HUSCAP

Surface chemistry and radionuclide anion immobilisation potential of phosphoric acid-activated metakaolin-based geopolymers

Xiaobo Niu, Yogarajah Elakneswaran *, Naoki Hiroyoshi

Division of Sustainable Resources,

Graduate School of Engineering, Hokkaido University,

North 13, West 8, Sapporo, Hokkaido, Japan, 060-8628

*Corresponding author

E-mail: elakneswaran@eng.hokudai.ac.jp

Tel: +81 11-706-7274

Abstract

Phosphoric-acid-activated metakaolin-based geopolymers (PGPs) have been investigated as promising options for the disposal of radionuclides. However, a lack of understanding of the surface chemical properties of PGPs has hindered further research into them and their application. This study explored the structure-related electrostatic properties and anion immobilisation potentials of PGPs via zeta potential measurements, structural characterisation, and leaching experiments. These findings suggest that acid activation triggers the geopolymerisation of metakaolin, resulting in new Al_x-PO units (x = IV, VI representing VI- and V-coordination), the ratio of which controls the surface charge of PGPs. PGPs possess a positive charge in the equilibrium pH range of approximately 2–5 and exhibit a maximum positive zeta potential at approximately pH 4. Under acidic conditions, the Al_{VI}-PO unit within the surface structure is released, decreasing the zeta potential as the pH decreases. In contrast, in alkaline environments, the Al_{VI}/Si-OH hydroxyl group loses protons, causing a decrease in the zeta potential with increasing pH. Furthermore, PGPs can effectively immobilise SeO_3^{2-}, SeO_4^{2-}, I^-, and IO_3^- anions through stabilisation/solidification (S/S). This immobilisation is primarily facilitated by electrostatic attraction between the anions and the positively charged surface of the PGPs. Importantly, the immobilisation process does not cause significant alterations to the matrix structure of the PGPs, even after solidification or subsequent leaching.

KEYWORDS: Acid-activated geopolymer; Metakaolin; Zeta potential; Immobilisation; Leaching

1. Introduction

The rapid development of contemporary society has brought about remarkable progress in industry and technology, but has also resulted in a series of significant environmental problems. The development of the nuclear industry is a prominent example [1, 2, 3]. Although the nuclear industry has brought tremendous energy and technological advancements to humanity, it has also produced vast quantities of contaminants, including radionuclides, which are not only released during nuclear accidents [4, 5, 6], but are also generated during normal nuclear facility operations, posing a significant threat to the natural environment and human health through their diffusion and accumulation in groundwater [7, 8, 9]. The radionuclides generated during nuclear operations, notably the cationic cesium-137 (^{137}Cs) and strontium-90 (^{90}Sr), as well as the anionic selenium-79 (^{79}Se) and iodine-129 (^{129}I), have received considerable attention. These radionuclides present formidable challenges in terms of proper disposal owing to their common forms in aqueous and soil environments (Cs^{+}, Sr^{2+}, SeO_3^{2-}/SeO_4^{2-}, and I^{-}/IO_3^{-}), high solubility and mobility, and long half-life (^{137}Cs, 30 years; ^{90}Sr, 28 years; ^{79}Se, 3.27×10^5 years; and ^{129}I, 1.57×10^7 years) [10, 11, 12]. At present, an important issue worldwide is handling and controlling the nuclear waste generated by the nuclear industry in an efficient, economical, and environmentally friendly manner.

Stabilisation/solidification (S/S) technology is widely used for solidifying hazardous waste into a stable, inert, and impermeable material [13, 14, 15]. This process involves mixing waste with a binder, such as cement, lime, or gypsum, to form a solid block, which reduces the environmental threat posed by hazardous waste [16, 17]. In recent years, the application of S/S technology to nuclear waste disposal has become an essential research topic. Low- to intermediate-level radioactive waste (LLW and ILW, respectively) can be stabilised and immobilised using S/S technology [18, 19]. This method has advantages over other disposal methods, such as reducing the volume of waste and increasing its density, making it easier to transport and store [20].

Geopolymers are a well-known class of inorganic polymers that have attracted significant attention owing to their low density, excellent thermal and mechanical properties, outstanding fire resistance, excellent chemical resistance, and strong resistance to permeability [21]. The use of geopolymers as potential substitutes for Portland cement in nuclear waste management, particularly in the application of S/S, has gained global attention [22]. Compared with conventional cementitious materials, geopolymer materials have demonstrated superior chemical durability owing to their three-dimensional framework structure derived from oxygen-linked aluminium and silicon, as well as their higher degree of silicate polymerisation [23].

Among the extensively studied geopolymers, alkali-activated aluminosilicate materials (AAMs) have been a common focus. The geopolymerisation process encompasses depolymerisation, polycondensation, and the formation of a gel network from an aluminosilicate precursor upon exposure to a highly alkaline solution or activator [24, 25]. AAMs are being actively investigated as a potential remedy for the long-term containment of contaminants, notably heavy metals and radionuclides [26, 27]. Owing to their large number of tetrahedral aluminium sites, AAMs have a permanent negative framework charge [28, 29]. Owing to this surface electrical property, AAMs are suitable for the uptake and adsorption of cationic radionuclides [30-34]. In our previous study, we found that Cs^{+} in AAMs formed complexes with zeolites in an alkaline environment and was eventually firmly immobilised in the AAMs [35]. Soonthornwiphat et al. [32] reported that AAMs exhibit excellent S/S performance for the encapsulation of Sr2+-loaded titanate ion exchangers. Tian et al. [36] successfully immobilised SeO_3^{2-} and SeO_4^{2-} into AAMs using S/S and surmised that electrostatic interactions were the primary association mode of selenium in geopolymers. However, as outlined in our previous study [30], the permanently negatively charged surface of AAMs demonstrates a significant capacity for the adsorption of cationic radionuclides while limiting the potential for the adsorption of anionic radionuclides. This raises concerns regarding the

reliability and durability of AAMs as solidification methods for anionic radionuclides, specifically selenium (^{79}Se) and iodine (^{129}I).

Acid-activated geopolymers are an intriguing alternative to AAMs, with phosphoric-acid-activated geopolymers (PGPs) being the most prominent and extensively studied [37]. The activation process involves the dealumination of an aluminosilicate precursor within a phosphoric acid activator, followed by the condensation of silicate tetrahedrons, culminating in the formation of $P(OAl)_x(H_2O)_{4-x}$ units connected to Si or Al [38]. The acid activators applied in PGPs, such as phosphoric acid, require lower activation temperatures and result in reduced CO_2 emissions compared with traditional alkaline activators, such as sodium hydroxide or silicate solutions [39]. Moreover, PGPs exhibit superior mechanical properties compared with AAMs [40-42]. Recently, the application of PGPs in the disposal of environmentally hazardous substances has gained increasing attention [31]. Liu et al. [43] introduced a new type of porous phosphoric acid-activated metakaolin-based geopolymer foam material and applied it to the removal of mixed pollutants (Pb(II), Cd(II), and Ni(II)) from aqueous solutions. Tome et al. [44] reported that phosphoric acid-activated volcanic ash-based geopolymers have an adsorptive potential for anionic (erochrome black T (EBT)) and cationic (methylene blue (MB)) dyes in water. Moreover, PGPs have recently received attention for their S/S applications. Pu et al. [45] found that acid-activated geopolymers better stabilise Pb^{2+} than cement- or alkali-activated geopolymers. However, to the best of our knowledge, studies on the S/S of radionuclides produced by PGPs are limited, especially for anionic radionuclides, such as selenium (^{79}Se) or iodine (^{129}I). The surface chemistry and electrical properties of PGPs require significant attention in the fields of anionic radionuclide stabilisation and solidification. Although AAMs have been extensively researched and acknowledged for their permanently negatively charged surfaces [19], there is a noticeable lack of comprehensive studies on these aspects of PGPs. This knowledge gap poses a significant disadvantage for exploring the potential of PGPs for the immobilisation of anionic radionuclides, highlighting the need for further research in this area.

This study aimed to understand the surface chemistry and structure-associated electrostatic properties of PGPs and explore their viability in the field of stabilisation/solidification of SeO_3^{2-}, SeO_4^{2-}, I^-, and IO_3^-. Notably, this is the first instance in which these specific substances have been considered for S/S implementation using PGPs. The surface properties of the PGPs were evaluated by X-ray photoelectron spectroscopy (XPS), zeta potential measurements, X-ray diffraction (XRD), nuclear magnetic resonance (NMR) spectroscopy, and inductively coupled plasma–optical emission spectroscopy (ICP-AES). The S/S capacities of the PGPs towards SeO_3^{2-}, SeO_4^{2-}, I^-, and IO_3^- were evaluated using XRD, inductively coupled plasma–mass spectrometry (ICP-MS), and Fourier-transform infrared spectroscopy (FTIR). This thorough analysis provided a deeper understanding of the surface chemistry of PGPs. Moreover, the findings of this study provide compelling evidence supporting the safe disposal of PGPs, especially those containing radionuclides or other potentially harmful environmental substances.

2. Experimental details

2.1. Materials

Metakaolin (MK) obtained from Sobueclay (Japan) was used to synthesise the PGPs. The chemical composition of the MK determined by X-ray fluorescence (XRF) is listed in **Table S1**; the molar ratio of SiO_2:Al_2O_3 in metakaolin is 1.91. Analytical-grade pure commercial phosphoric acid (WAKO (Japan), 85 wt. % H_3PO_4) and ultrapure water (TRUSCO, Japan) were used to produce a phosphoric acid solution, which was used as an acidic activator for the synthesis of PGPs. KNO_3 (KANTO, >99%), KOH (KANTO, >86%), and HNO_3 (KANTO, 61%) were used to adjust the pH and ionic strength of the solutions. In addition, the non-radiological isotopes K_2SeO_3, K_2SeO_4, KI, and KIO_3 were selected as the simulated radionuclide sources and purchased from WAKO (Japan).

2.2. PGPs synthesis

The PGPs were prepared by mechanically mixing stoichiometric amounts of metakaolin with a sufficient quantity of an acidic-activated solution, yielding a solid-to-liquid mass ratio of 1. Acidic-activated solutions were prepared by diluting 85 wt. % phosphoric acid, and detailed information on the PGP sample compositions is shown in **Table 1,** where Si and Al were determined through the molar contents of SiO_2 and Al_2O_3 in metakaolin (**Table S1**), and P represented the molar content of H_3PO_4 from phosphoric acid. To achieve efficient curing while mitigating thermal cracking, a two-stage curing protocol was implemented after sealing the homogeneous slurry with parafilm [38]. This procedure involved an initial pre-curing phase at 40 °C for 24 h, succeeded by a subsequent 24-h curing phase at 60 °C. Afterwards, PGPs were ground to a particle size of less than 150 μm and stored in vacuum bags for further analysis.

Table 1. The molar ratio of the Si, Al and P in the PGPs, and the concentration and mass fraction of acid activator solutions.

Samples	Si/Al	P/Al	P/H_2O	H_3PO_4 (M)	H_3PO_4 (wt. %)
PGP1	0.956	1.025	1.042	14.659	85
PGP2	0.956	0.821	0.391	10.305	68
PGP3	0.956	0.615	0.191	6.893	51
PGP4	0.956	0.410	0.094	4.147	34

2.3. Surface chemical properties experiments

2.3.1. Structural characterisation of PGPs

A Rigaku X-ray diffractometer (MultiFlex, Rigaku, Japan) was used to characterise the synthetic samples with CuKα radiation, scanning from 2θ=5–70° with a scan speed of 6.5° per min and a step size of 0.02°. The solid-state magic angle spinning (MAS) NMR spectra of the PGPs were acquired using a Bruker

500 MHz spectrometer equipped with an 11.74T magnet. ^{29}Si MAS NMR spectra were collected at 99.4 MHz using a φ3.2-mm probe with a pulse width of 1.5 μs (30°) and spinning speed of 5 kHz, and a total of 2800 scans were recorded with 20-s recycle delay for each sample. For ^{27}Al MAS NMR experiments, a φ2.5-mm probe operating at 130.4 MHz with a pulse width of 5.8 μs (90°), spinning at 30 kHz, was used to record a total of 3600 scans, with a 5-s recycle delay for each sample. The chemical shifts for both ^{29}Si and ^{27}Al nuclei were referenced to hexamethylcyclotrisiloxane ($C_6H_{18}O_3Si_3$) and an $AlCl_3$ solution (1 mol/L).

2.3.2. Zeta potential measurement

A zeta potential and particle size analyser (ELSZ-1000ZS) was used to measure the zeta potential of the PGPs in neutral (pH = 7) and acidic/alkaline (pH: 2–12) solutions with ionic strengths of 10 and 100 mM, respectively, and the solid/liquid ratio of the suspension was set to 1 g/L. Moreover, the zeta potential of PGP2 changed with time in the SeO_3^{2-}, SeO_4^{2-}, I^-, and IO_3^- solutions. The initial anion concentration was 1 mM and the pH and ionic strength were set to 4 and 10 mM, respectively, to simulate the internal environment of the PGP2 matrix. Solutions with the same ionic strength and pH, but without SeO_3^{2-}, SeO_4^{2-}, I^-, and IO_3^-, were used as controls. The zeta potential was measured after immersion for 1, 3, 7, 14, 21, and 28 d. Among the various solutions used to examine the zeta potential, KNO_3 was selected to modulate the ionic strength, whereas KOH and HNO_3 were employed to regulate the pH.

2.3.3. Component changes of PGPs in the aquatic environment

The quantities of P, Si, and Al dissolved from the PGPs in water, acidic, and alkaline solutions were determined using inductively coupled plasma–atomic emission spectroscopy (ICP-AES; SPECTROBLUE, Hitachi, Japan). The ICP-AES analysis covered the wavelength range of 165–770 nm. The pH of the solutions was measured using a pH meter (AS ONE Ltd., Japan), specifically the AS800

model. The solid/liquid ratio of all the suspensions was set to 1 g/L, the ionic strength of the acidic and alkaline solutions was set to 10 mM using KNO_3, and the pH was controlled using KOH and HNO_3.

2.3.4. XPS measurement

X-ray photoelectron spectroscopy (XPS) analysis was performed using a JPS-9200 (JEOL, Japan) for detailed chemical composition characterisation of the PGPs before and after immersion in water or pH solutions. Photoelectron emission was excited by the monochromatic Mg Kα line with a photon energy of 1253.6 eV. Detailed spectra of each sample were obtained using a narrow scan with an energy step of 0.1 eV and a dwell time of 100 ms. Charging compensation was performed using a neutralising electronic gun under a constant current and voltage. The binding energy axis was adjusted according to the position of the C 1s line.

2.4. Stabilisation/solidification (S/S) and leaching experiment

2.4.1. Preparation of solidified wasteform

Based on the structure and properties (refer to Section 3), the PGP2 samples were selected as the matrix to solidify SeO_3^{2-}, SeO_4^{2-}, I^-, and IO_3^-. Predetermined quantities of K_2SeO_3, K_2SeO_4, KI, and KIO_3 were dissolved in four separate batches of the acid activator solutions. These solutions were then individually mixed with metakaolin to achieve a specific ratio of 1 mmol of the intended anion per 100 g of PGP slurry. The fresh mixture was cast into a cylindrical mould with a height and inner diameter of 1.5 and 1.3 cm, respectively, after stirring, obtaining a 3.6-g (± 0.02-g) specimen containing approximately 36 μmol of target anions. These specimens were sealed with parafilm and underwent two-stage curing as the original PGPs.

2.4.2. Leaching experiments

Leaching experiments were conducted after curing using the ANSI/ANS-16.1-2003 standard test (American Nuclear Society, 2004). Each specimen was immersed in 88 mL of deionised water as the leachate (the ratio of the leachate volume to the specimen surface area was 10 mL/cm^2), as shown in **Fig. 1**. The leachate was replaced entirely after cumulative leaching times of 2 h and 9 h and 1, 2, 3, 4, 5, 7, 14, 21, and 28 d at room temperature (approximately 20 ℃) from the onset of the test. The leachates were then analysed at each time point to determine the released SeO_3^{2-}, SeO_4^{2-}, I^-, and IO_3^- contents from the PGP2 matrix. The specimens were recovered after 28 d of leaching and then ground into powder with particles smaller than 150 μm for solid analysis after 3 d of drying in a 40 ℃ thermostat.

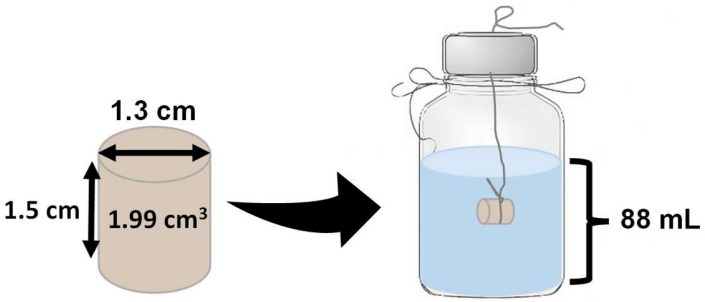

Fig. 1. Schematic of leaching experiments

The leachates obtained from the leaching experiments were analysed using ICP-MS (iCap Q ICP-MS, Thermo Scientific, USA; detection limit 0.01–10 ppb). SeO_3^{2-} and SeO_4^{2-} were measured using the yttrium internal standard method with ultrapure water as a solvent. All solutions used for ICP-MS measurements were spiked with 1% HNO_3 (approximately 60 wt. %) for sample protection. The measurement of I^- and IO_3^- was conducted with the application of the caesium internal standard method using 0.5% tetramethylammonium hydroxide (TMAH) as a solvent, and all solutions used for ICP-MS measurements were spiked with 1% Na_2SO_4 (1 wt. %) for sample protection. The anion-solidified PGP2 samples before and after the leaching experiment were characterised via Fourier-transform infrared (FTIR) spectroscopy (JASCO670, Japan) at a constant spectral resolution of 4 cm^{-1}. Solid samples were

recorded in the wavenumber range of 400–2000 cm^{-1} after dilution with KBr and pressing into tablets. In addition, XRD measurements were conducted using the same method for all solid samples before and after the leaching experiments.

3. Results and discussion

3.1. Structural properties of PGPs

3.1.1. XRD

Figure 2 shows the X-ray diffraction patterns of the metakaolin precursor and PGPs obtained after a two-stage curing process using different concentrations of phosphoric acid as the activator. The XRD pattern of the metakaolin precursor exhibited a broad hump in the 2θ range of 15–30°, along with minor crystalline phase peaks of mullite and quartz, which were retained in all concentrations of acid-activated PGPs as an inert phase. This indicates that acidic activators encounter difficulties in dissolving and activating Al and Si, which have already formed stable crystalline structures. Upon activation with acidic activators, the broad hump of all samples shifted towards 17–35°, indicating that the PGPs had a more disordered short-range structure with relatively shorter interatomic distances compared with the metakaolin precursors. Similarly, the hump at less than 15° in the pattern of the metakaolin precursor, which represented a large interatomic distance (cannot be shown for less than 5°), also shifted towards 15° upon activation with acidic activators. This shift was most pronounced in the PGP1 samples activated by the highest concentration of the acid activator. Among the four types of PGPs, PGP2 exhibited the highest reactivity and densest structure, as evidenced by its largest relative variation and fullest hump in the high-diffraction-angle region. This suggests that a concentration of approximately 10.3 M may be optimal for the phosphoric acid activator, consistent with previous findings [46].

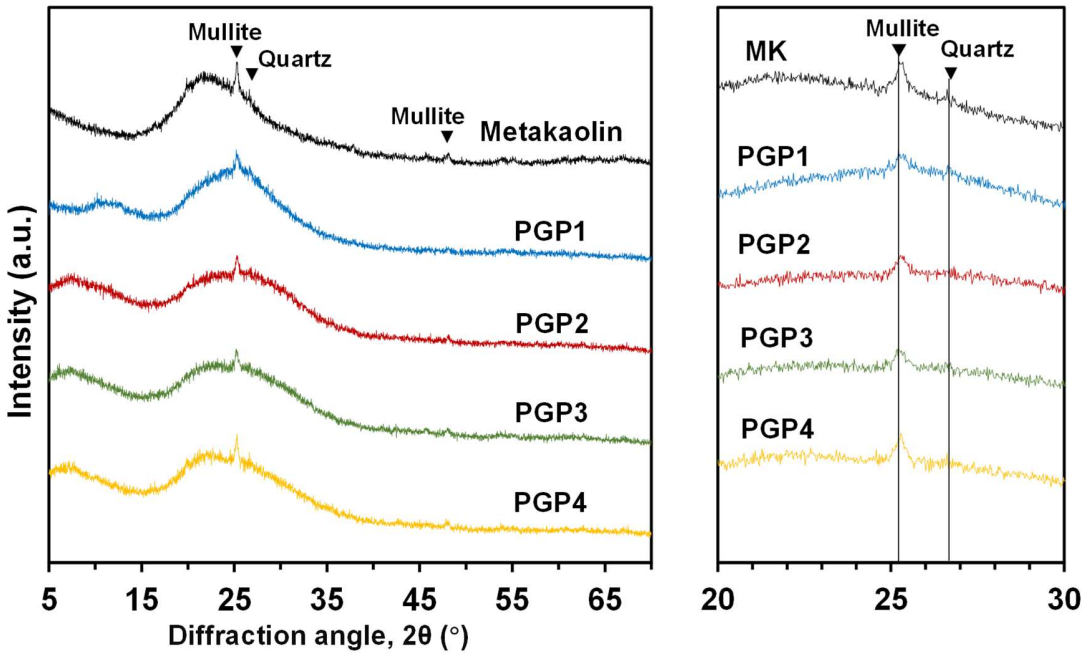

Fig. 2. X-ray diffraction (XRD) patterns of metakaolin and PGPs.

3.1.2. ^{29}Si NMR

In cementitious materials, silicon sites are often labelled using the notation Q^n(mAl), where Q represents Si in tetrahedral coordination, and n and m denote the number of tetrahedral atoms and Al atoms bonded to Si, respectively. The values of n and m range from 0 to 4, indicating that Si is connected to n other tetrahedral atoms, of which m is Al, through O bridges. Based on this labelling system [45], **Fig. S1(a)** illustrates the correspondence between the ^{29}Si nuclei in the different chemical environments of cementitious materials and their typical chemical shift ranges. As the number of bridged oxygen atoms around the Si increases, the chemical shift gradually shifts toward the higher-field region. This suggests that electromagnetic shielding is enhanced. In contrast, an increase in the substitution of aluminium atoms around the silicate tetrahedra resulted in reduced electromagnetic shielding of the Si nuclei, leading to a displacement of the Q^4(mAl) chemical shift towards a lower field.

Figure 3 shows the ^{29}Si NMR spectra and their corresponding individual Gaussian peaks after deconvolution using the Gaussian amplitude function. The main chemical environment of Si in phosphoric- acid-activated metakaolin PGPs was found to include Q^0, Q^1, Q^2(1Al), Q^3(1Al), Q^4(4Al), Q^4(3Al), Q^4(2Al), Q^4(1Al), and Q^4(0Al), which were positioned at chemical shifts around approximately −68 ± 5, −76 ± 5, −85 ± 3, −86 ± 4, −88 ± 3, −94 ± 4, −100 ± 5, −105 ± 4, and −115 ± 4 ppm, respectively [38]. However, it is important to note that structural units, such as Q^4(4Al), Q^4(3Al), Q^4(2Al), Q^4(1Al), and Q^4(0Al), may not necessarily correspond to a single chemical shift peak due to the significant overlap between broad resonances in disordered solid phases, particularly for silicate tetrahedrons. Consequently, multiple deconvolution techniques have been utilised to achieve a more accurate fit.

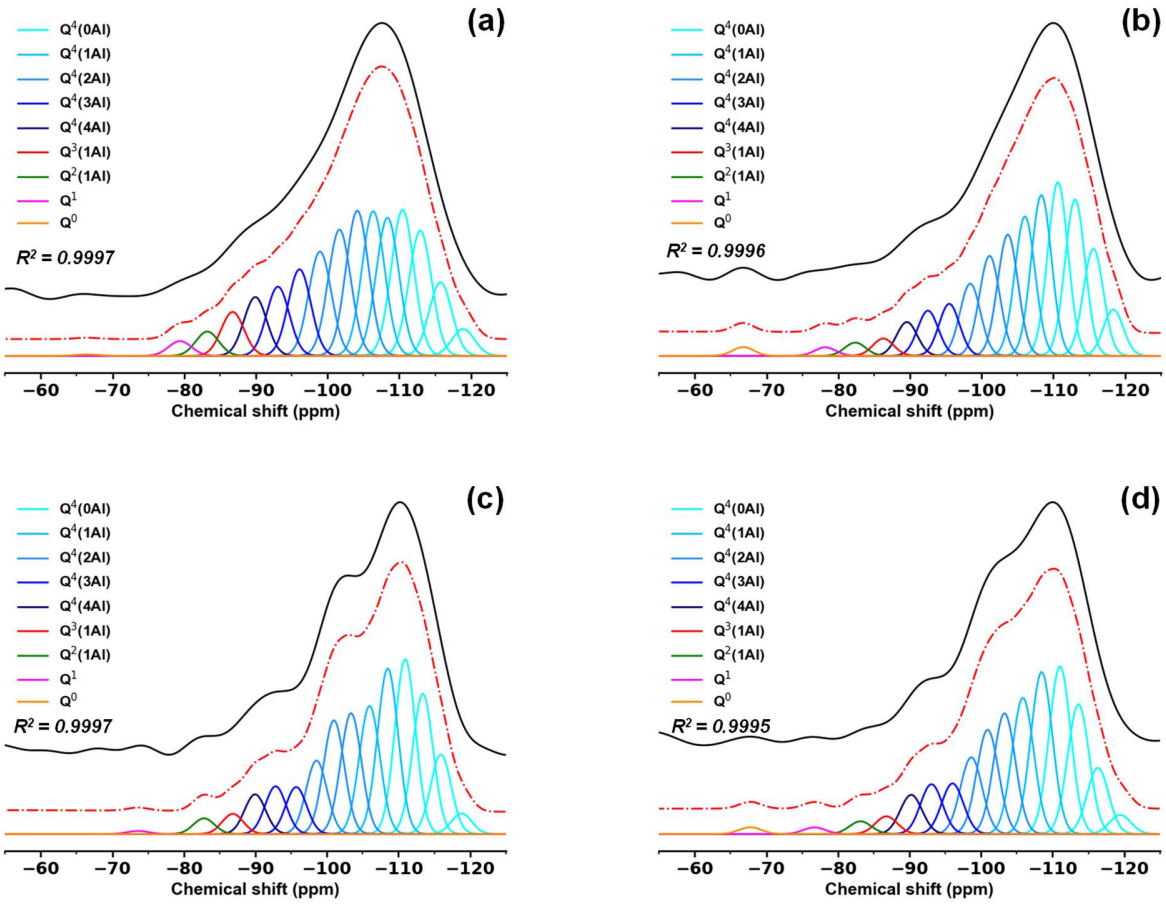

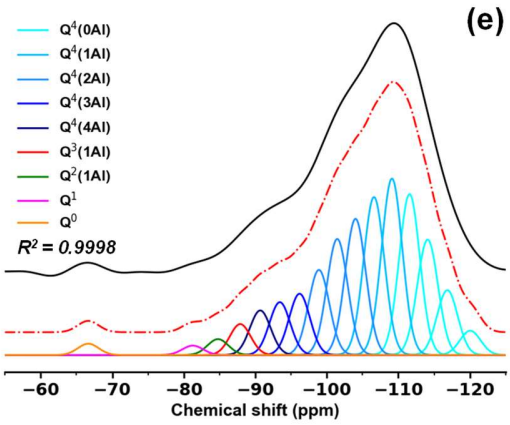

Fig. 3. Deconvolution results of ^{29}Si NMR spectra for MK and the PGPs after curing: (a) MK, (b–e) PGP1, PGP2, PGP3, and PGP4, respectively.

Figure 4 shows the molar fractionation of Si in different chemical environments in MK and PGPs derived from ^{29}Si NMR spectra deconvolution results. The Q^4(0Al) units were found to be the dominant species in a given PGP sample, and their proportion increased with the concentration of the acid activator. In contrast, the number of remaining silicate tetrahedra decreased as the concentration of the acid activator increased. This is because higher concentrations of acid activators caused more significant dealumination of MK. This dealumination process promoted the condensation of silicate tetrahedrons, increasing Q^4(0Al). It is also noteworthy that the Q^4 (1Al) units of all the PGPs increased to varying degrees compared with MK. This is because Q^4(1Al) is also the product of the dealumination of higher-Al-content silicate tetrahedrons, and higher concentrations of the acid activator further enabled the dealumination of Q^4(1Al), resulting in more Q^4(0Al).

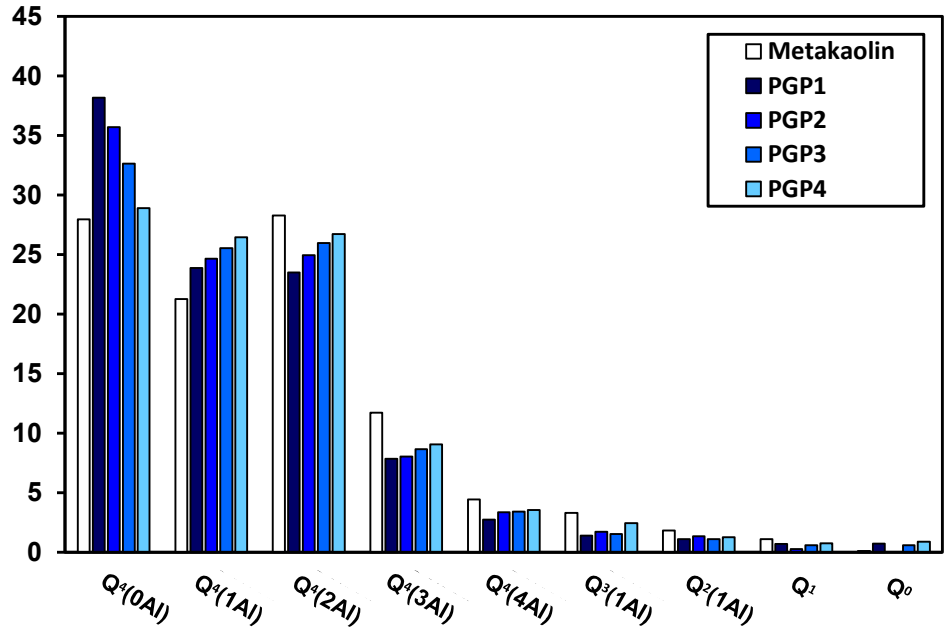

Fig. 4. Molar proportions of Si structural units in MK and PGPs quantified through the ^{29}Si NMR deconvolved spectra.

3.1.3. ^{27}Al NMR

Figure S1(b) illustrates the primary features of the ^{27}Al chemical shift variation observed in most types of porous aluminosilicate solids, where Al typically exists in IV-, V-, and VI-fold coordination structures [47]. As the number of coordination structures around the Al atom increased, the chemical shift gradually increased to higher fields. However, the chemical shifts of Al with the same coordination number varied depending on the type of atoms connected to it via bridging oxygen atoms. In general, Al_x-OP has a chemical shift closer to the high-field range than Al_x-OSi/OH because P is less electronegative than O and Si. The deconvolution strategy for ^{27}Al in the PGPs sample was different from that for ^{29}Si, because ^{27}Al (S = 5/2) is a class of quadrupolar nuclei (S > 1/2), and quadrupolar interactions must be considered in the process of simulating the spectra [48]. As a result, deconvolution and simulation of ^{27}Al NMR spectra were achieved by combining multiple Pearson IV functions [49].

The deconvolution results of the ^{27}Al NMR spectra of MK and PGPs are shown in **Fig. 5**. The chemical environment of Al in metakaolin was mainly composed of IV- and V-coordinated structures, with a small fraction of VI-coordinated structures. Upon activation with an acid activator, the original VI-coordinated Al species linked to Si/OH in MK disappeared, and the V-coordinated Al species decreased significantly. Meanwhile, new IV-, V-, and VI-coordinated Al species linked to OP were generated. The intensity corresponding to the VI-coordinated Al species linked to -OP increased significantly with increasing acid activator concentration.

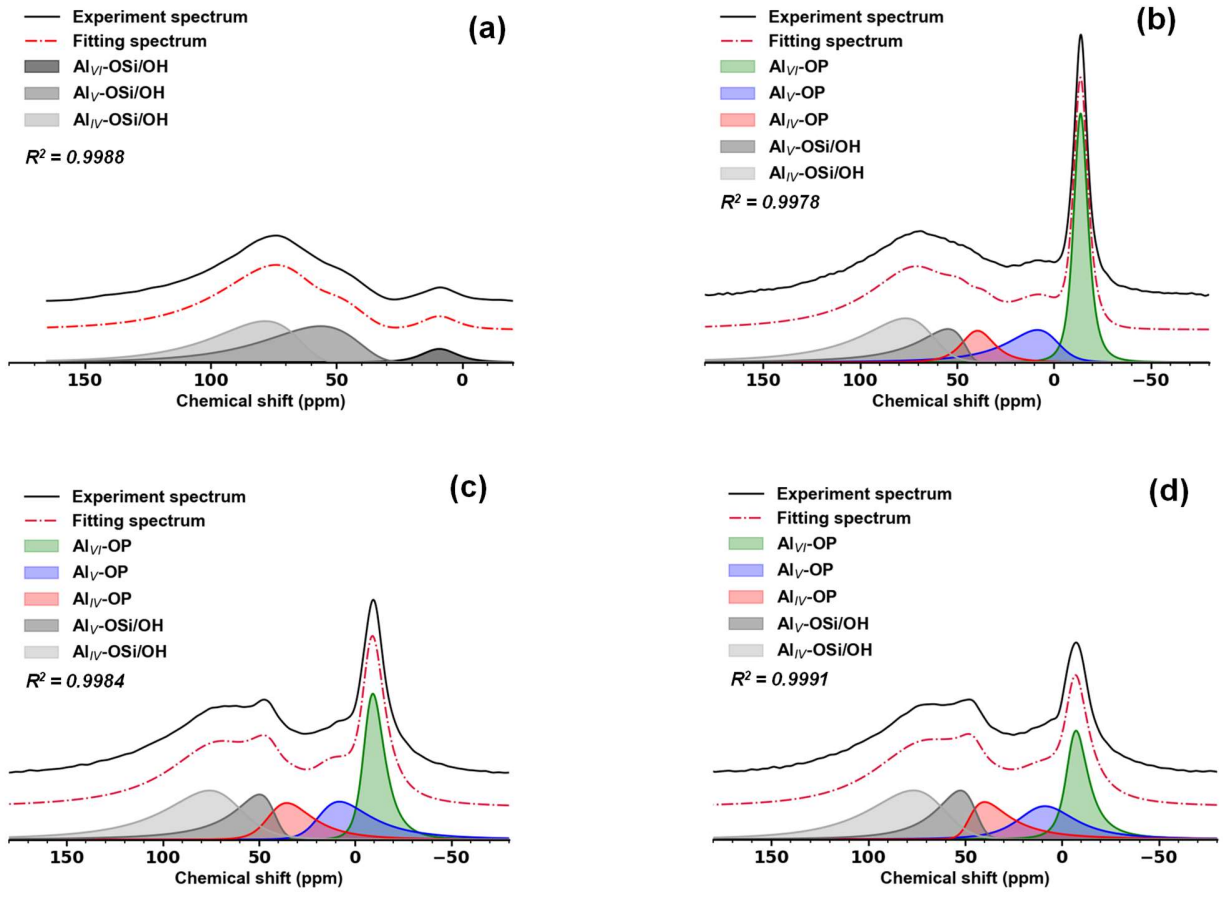

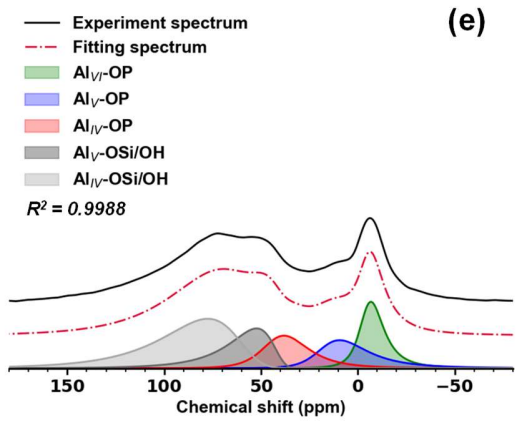

328

329 **Fig. 5.** Deconvolution results of ^{27}Al NMR spectra for MK and the PGPs after curing. (a) MK, and (b–

330 e) PGP1, PGP2, PGP3, and PGP4, respectively.

331

332 **Figure 6** shows the molar proportion of Al in metakaolin and PGPs for each chemical structural unit

333 based on ^{27}Al NMR deconvolution. Upon the activation of metakaolin to form PGPs, the Al$_{VI}$-OSi/OH

334 component was eliminated, while notable reductions were observed in the Al$_{V}$-OSi/OH and Al$_{IV}$-OSi/OH

335 components. The reductions in the latter two were positively correlated with the concentration of the acid

336 activator. The proportion of Al$_{VI}$-OP, a novel structural unit generated in PGPs, increased significantly

337 with increasing activator concentrations. In contrast, the proportions of the other two newly formed

338 structural units, Al$_{IV}$-OP and Al$_{V}$-OP, decreased with increasing acid activator concentration. Although

339 PGP4, with the lowest concentration of acidic activator, exhibited the lowest percentage of Al$_{V}$-OP of

340 all PGPs, this may be attributed to the insufficient concentration of the acid activator, which hinders the

341 effective progress of dealumination and thus the formation of Al$_{V}$-OP, to an extent. These findings

342 indicate that higher concentrations of acid activators facilitate the dealumination process of metakaolin,

343 but only favour the formation of new structural units of Al$_{VI}$-OP.

344

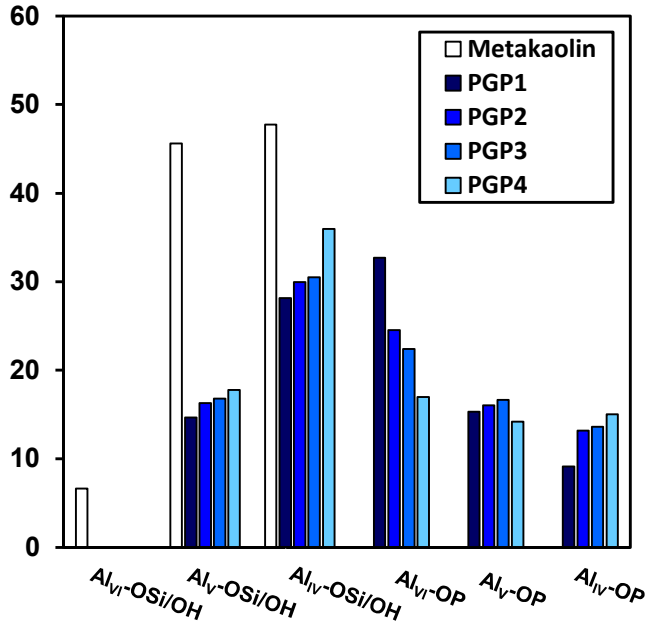

Fig. 6. Molar proportions of Al coordination structural units in MK and PGP 1–4 quantified through the ^{27}Al NMR deconvolved spectra.

3.2. Zeta potential

The pH plays a critical role in influencing the surface electrostatic properties of materials. To investigate the zeta potential behaviour of the PGPs under different pH conditions, the PGP powder was immersed in solutions spanning the pH range from acidic to basic (pH 2–12). The pH and zeta potential values of PGP1–PGP4 after reaching equilibrium in a neutral solution (pH 7) are presented in **Table 2**. At equilibrium, the pH values exhibited varying degrees of reduction, gradually decreasing with increasing concentrations of the acid activator (PGP4–PGP1), whereas the zeta potential showed a corresponding gradual increase. The influence of pH on the zeta potential of the PGPs in acidic and basic solutions is shown in **Fig. 7.** Similar to the neutral solution (**Table 2**), an overall decrease in the solution pH was observed after equilibrium compared with the initial pH setting. This decrease could be attributed to the acidic nature of the PGPs activated by the acid activator. The magnitude of the pH reduction upon the introduction of these materials into the solution depended on the concentration of the acid activator. The

zeta potential values of the PGPs demonstrated an initial increase, followed by a subsequent decrease with variations in pH, which was observed in both the 10- and 100-mM ionic strength solutions. The zeta potential curve of the PGPs in the solution with 100-mM ionic strength appeared flatter than that in the solution with 10-mM ionic strength. This flattening can be attributed to the formation of a thinner electrical double layer (EDL) on the surface of the PGP particles in the higher-ionic-strength solution, resulting in a lower absolute value of the zeta potential for the same charge amount [50]. Progressive rightward displacement of the zeta potential peaks was observed from PGP1–PGP4 in solutions of both ionic strengths. These peaks corresponded exactly to the pH and zeta potential values of the PGPs at equilibrium in a neutral solution with an initial pH of 7. The PGPs exhibited peak positive zeta potentials at equilibrium pH levels. Deviations from this pH value resulted in a gradual decrease in the zeta potential in either direction.

Table 2. pH and zeta potential of PGPs at equilibrium in neutral solution.

	PGP1	PGP2	PGP3	PGP4
pH-10 mM	3.76 ± 0.01	4.05 ± 0.02	4.29 ± 0.03	4.53 ± 0.02
Zeta potential (mV)-10 mM	40.02 ± 0.04	36.98 ± 1.27	33.64 ± 0.57	25.18 ± 0.79
pH-100 mM	3.66 ± 0.03	3.98 ± 0.04	4.24 ± 0.02	4.41 ± 0.04
Zeta potential (mV)-100 mM	24.95 ± 0.93	20.08 ± 0.25	19.55 ± 0.91	14.88 ± 0.17

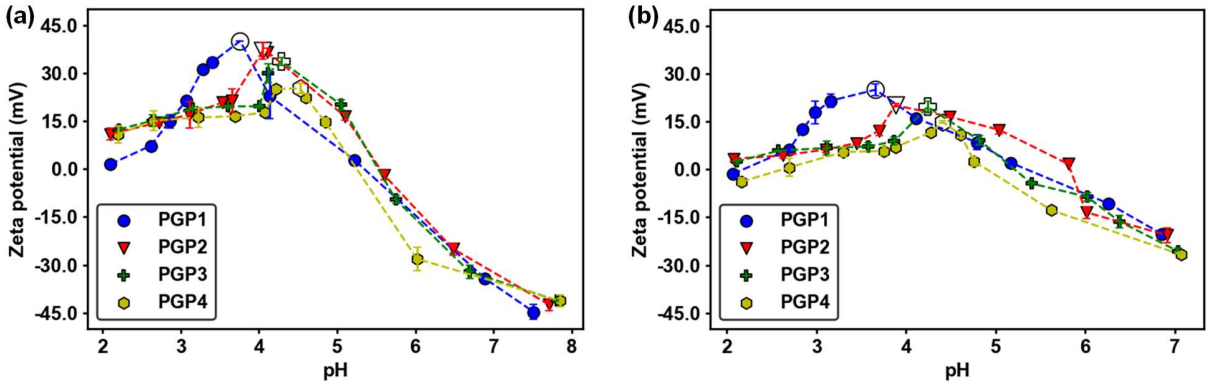

376

377 **Fig. 7.** Zeta potential of PGPs in NO_3^- solutions of (a) 10- and (b) 100-mM ionic strength at various pH
378 values after equilibrium (empty symbols identify testing in a pH 7 solution).

379

380 The coordination state of Al significantly affects the surface charge of aluminosilicate materials. For
381 example, the surface is negatively charged in zeolites and AAMs where IV-coordinated Al dominates
382 [51, 52]. This is because the tetrahedral Al_{IV} sites always provide Brønsted acidity, resulting in a
383 negatively charged surface [53]. In contrast, the octahedral Al_{VI} sites are amphoteric in nature. In acidic
384 environments, they can provide Brønsted basicity and a positive charge after binding to protons, whereas
385 in alkaline environments, they can provide Brønsted acidity and a negatively charged surface [54].
386 **Figure 8** shows the zeta potential of the PGPs as a function of the Al_{VI}/Al_{IV} ratio, as determined by ^{27}Al
387 NMR analysis in a neutral solution. The surface charge of the PGP sample was positively correlated with
388 the Al_{VI}/Al_{IV} ratio in its structure, which can be explained by the above theories.

389

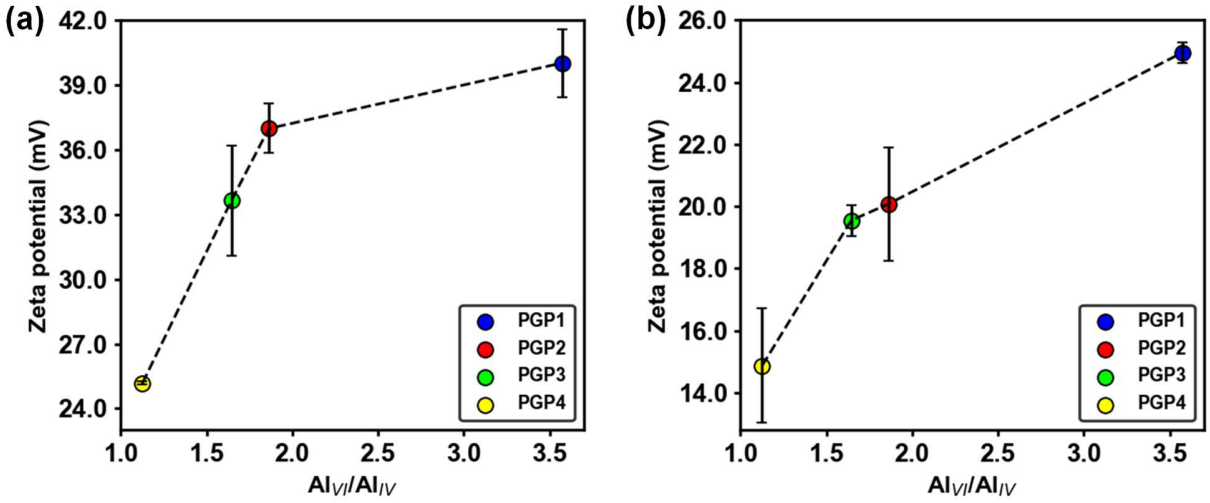

Fig. 8. Zeta potential of PGPs in neutral solution with ionic strengths of (a) 10 mM and (b) 100 mM as a function of Al_{VI} / Al_{IV} molar ratio.

Figure 9 presents the time-dependent zeta potentials of PGP2 in four different anion solutions. Following a day of immersion, only the zeta potential of PGP2 in SeO_4^{2-} was significantly lower than that in the control group. Subsequently, the zeta potentials gradually decreased to varying extents, with a noticeable distinction observed after 7 d, demonstrating the significant electrostatic attraction of PGP to all anions. Equilibrium was achieved after approximately 14 d, with only a slight decrease observed at 28 d. The reduction in zeta potential after reaching equilibrium followed the order of SeO_4^{2-}>SeO_3^{2-}>I^->IO_3^-. Charge density plays a crucial role in the variation of the zeta potential upon adsorption onto colloidal surfaces. Even among ions with the same valence state, those with larger ionic sizes and lower charge densities exhibited a relatively limited influence on the zeta potential [55]. Although the ionic sizes of SeO_4^{2-} and SeO_3^{2-} are comparable, the latter acquires protons in acidic surroundings, forming $HSeO_3^-$, thus exhibiting a lower charge density than SeO_4^{2-}. However, the charge density of IO_3^- with oxygen atoms is considerably lower than that of I^-, resulting in a change in the relatively low zeta potential.

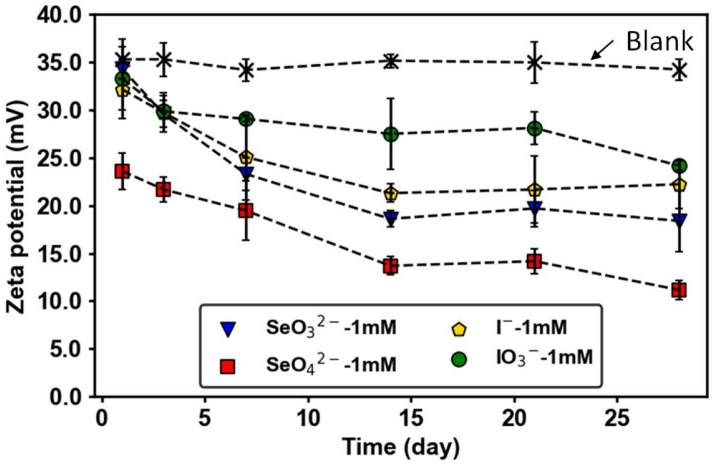

Fig. 9. Zeta potential of PGP2 in anionic solutions of 1 mM concentration with time (all solutions had a pH of approximately 3.6 ± 0.2).

3.3. Surface changes in the aqueous environment

3.3.1. Component changes

To study the surface behaviour of the PGPs in an aqueous environment, the change in the surface composition of the PGPs after immersion in water was investigated. **Figure 10(a)** shows the percentages and relative proportions of Al, Si, and P in the raw materials. In all PGPs, the proportions of Al and Si remained consistent, given that MK was the source. However, the proportion of P decreased as the acid activator concentration decreased. The composition of the ground PGP powder is presented in **Fig. 10(b)**. The surfaces of the PGPs showed a higher Si content and lower P and Al contents with decreasing acid activator concentration, except for PGP1, which had the second-lowest Al content after PGP4. Compared with the raw material, as determined by the experimental design composition (**Fig. 10(a)**), it is evident that all PGPs, except PGP4, exhibited reduced levels of Al and increased levels of P on their surfaces. This can be attributed to the dealumination and penetration of P during geopolymerisation, which resulted in a significant number of defective sites in the original Si-O-Al structure. During grinding, these sites were easily fractured, forming the surface of the obtained powder. Upon immersion in water (**Fig. 2S(a)**),

425 significant amounts of Al and P leached from the surface of the PGPs, whereas little Si was detected in
426 the leachate. This indicates the inability of the acid activator to dissolve Si in MK and the presence of
427 large amounts of extra-framework Al (EFAL) and free PO_4^{3-} on the surface of the PGPs. Furthermore,
428 analysis of the surface Al, P, and Si contents after water immersion revealed that the relative Al and P
429 contents on the surfaces of all PGPs were similar after water immersion (**Fig. 10(c)**), which may be
430 attributed to the preference of Al and P for the formation of Al-O-P in the structure [38]. Moreover, the
431 Si content increased from PGP2 to PGP4, with PGP1 displaying a Si content comparable to that of PGP4.
432 This can be explained by the fact that a suitable concentration of the acid activator (PGP2) facilitates the
433 geopolymerisation process, resulting in the formation of more Al-O-P units within the structure. In
434 contrast, an excessive concentration of an acid activator (PGP1) may promote a rapid dealumination
435 process and the accumulation of Al^{3+} around the metakaolin particles, thereby impeding the reaction.
436 Therefore, combining the XRD and NMR analysis results, PGP2 was selected as the sample in this
437 context for further study.
438
439 When PGP2 was immersed in an acidic environment, Al leaching increased significantly as the pH
440 decreased (**Fig. 2S(b)**). Conversely, in an alkaline environment, the leaching of Al remained consistently
441 low and was independent of the pH, with fluctuations presumably due to Al^{3+} precipitation from the basic
442 pH. Correspondingly, as shown in **Fig. 10(d)**, the concentrations of Si, Al, and P on the surface of PGP2
443 exhibited distinct trends when exposed to acidic solutions at different pH levels. Specifically, as the
444 solution pH decreased, the proportion of Si gradually increased, whereas the proportions of Al and P
445 decreased. In contrast, the individual components remained stable after immersion in an alkaline solution.
446

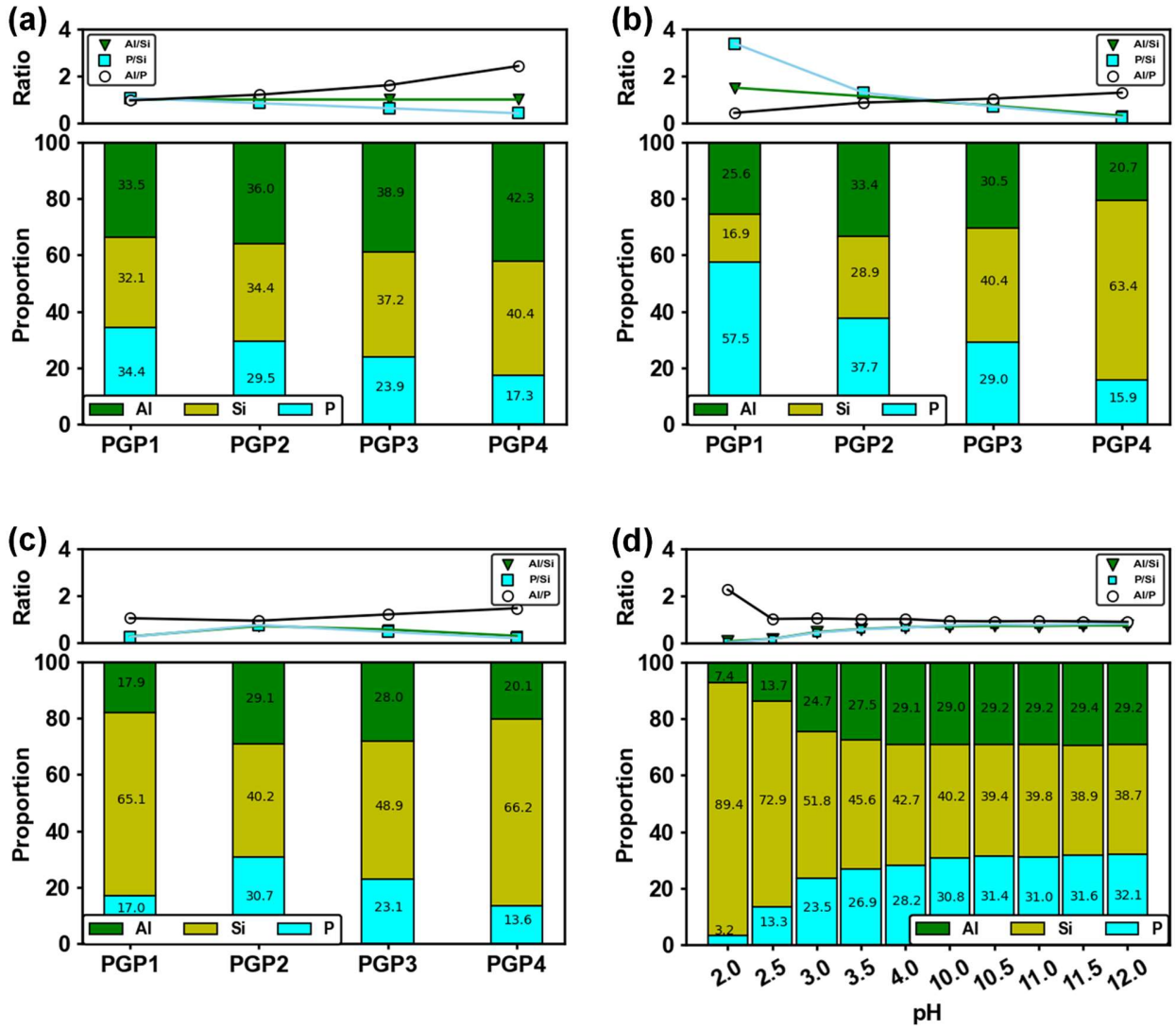

Fig. 10. Proportion and relative molar ratio of Al, Si, and P in (a) raw materials, (b) PGPs before water immersion, (c) PGPs after water immersion, and (d) proportion and the relative molar ratios of Al, Si, and P in the PGP2 sample with pH variation.

3.3.2. XPS spectroscopy analysis

X-ray photoelectron spectroscopy (XPS) was employed to examine the changes in the surface chemistry of the PGP2 samples following their immersion in aqueous solutions with varying pH. The resulting XPS spectral changes of Al 2p, Si 2p, O 1s, and P 2p of the PGP2 samples in acidic and alkaline solutions with progressive pH modification are shown in **Fig. 3S(a)** and **(b)**, respectively. In acidic solutions (**Fig.**

458 **3S(a)**), the intensities of Al 2p and P 2p decreased gradually with decreasing pH, which was attributed
459 to the dissolution and leaching of Al and P from the surface of PGP2 under acidic conditions (**Fig. 2S(b)**).
460 Furthermore, as the pH decreased, the binding energies of Si 2p and O 1s gradually increased. This trend
461 can be attributed to the dissolution of Al and P from the surface structure of PGP2, resulting in a higher
462 electron cloud density around the Si and O atoms. In alkaline solutions (**Fig. 3S(b)**), no significant
463 chemical composition or structural changes were observed in any of the XPS spectra with increasing pH.
464 These results align with prior compositional analyses (**Fig. 10(d)**) and suggest that PGP2 can maintain a
465 more stable surface chemical structure in an alkaline environment than in an acidic environment.
466
467 To achieve a more comprehensive analysis of the changes in the surface chemical structure of PGP2
468 under different pH conditions, high-resolution XPS spectra at three initial pH values (2, 7, and 12) were
469 deconvoluted using a Gaussian amplitude function and compared (**Fig. 11**). Furthermore, the different
470 chemical states of the PGP2 sample were quantified and the results are presented in **Table 3**. The Al 2p
471 spectrum of PGP2 exhibited two peaks located at 75.15 and 76 eV. As established in previous studies
472 [56, 57], the peak at 75.16 eV is attributed to $AlPO_4$ linkages, whereas the peak at 76 eV corresponds to
473 Al-O-Si bonds. In the neutral and alkaline solutions, no significant differences in Al 2p contributed to
474 either chemical environment. However, in acidic solutions, both peaks were significantly weakened,
475 although the relative intensity of the Al-O-Si peak was higher. These results indicate that the Al-O-P
476 bond in AlPO4 is more vulnerable to breakage in acidic environments than the Al-O-Si bond.
477 Consequently, the dealumination of the PGP2 surface was primarily caused by the breakage of the Al-
478 O-P bond.
479
480 The Si 2p spectrum was deconvoluted into three components. The peak at a binding energy of 102 eV
481 was associated with Si-O-Al [54], whereas the peaks at approximately 103.1 and 104 eV were attributed
482 to Si-O-P and Si-O-Si, respectively [58, 59]. The presence of these three stable peaks in neutral and

alkaline environments indicates the relative stability of the chemical environment and the composition of Si on the PGP2 surface, similar to the behaviour observed for Al. However, in an acidic environment, the Si 2p peak of Si-O-P disappeared, leaving only a faint Si-O-Al peak. This suggests that dealumination of the PGP2 surface in an acidic environment is more likely to occur through the removal of P-linked Al from Si-O-P-Al than from Si-O-Al.

The O 1s spectrum of PGP2 was deconvoluted into four main components. The peak at 531 eV could be attributed to P-O-P bonds from the network structure or P=O bonds from the PO_4^{3-} functional groups [59, 59]. The binding energy peaks at 532.1 and 533 eV corresponded to the bridging oxygen in Si-O-Al and Si-O-Si, respectively [54, 61]. The peak at 534 eV corresponded to the O 1s binding energy of terminal Si (Si-OH) groups [62]. The O 1s peaks of Si-O-Si on the PGP2 surface exhibited a relatively stable content in both neutral and alkaline environments, while the increase under acidic environments was due to dealumination. Correspondingly, the O 1s contribution to Al-O-Si decreased significantly in acidic environments and remained almost constant in neutral and alkaline environments. Although the O 1s peak corresponding to P-O-P (P=O) was relatively weak, a reduction could still be observed in acidic environments. The O 1s peak corresponding to Si-OH gradually decreased from low to high pH, which can be attributed to the decrease in Si-OH at the defective sites or terminal Si resulting from broken P-O-Si and Al-O-Si bonds. The $Si\text{-}O^-$ at these fracture points had a strong affinity for accepting protons from the acidic environment to form Si-OH. In an alkaline environment, the hydroxyl radical ions in the solution reacted with Si-OH on the surface of PGP2, which is a common reaction observed in silicate materials in alkaline environments [63]. This reaction weakened the O 1s XPS peak intensity of Si-OH. Notably, as the intensity of the O 1s peak corresponding to Si-OH decreased, a new peak appeared at a binding energy of approximately 534.5 eV, which was previously identified as O 1s in $Si\text{-}O^-$ [64]. This result also provides evidence that the Si-OH groups on the surface of PGP2 undergo deprotonation to form $Si\text{-}O^-$ in alkaline environments.

In the P 2p spectra, only one component was discerned on the PGP2 surface in the natural and alkaline environments. This component is likely a mixture of Si-O-P bonds, Al-O-P bonds, and variations in the O-P-O and P=O bond content [65]. In such cases, P exists in a crosslinking-type chemical environment that connects Al and Si in tetra-coordinated P [66]. Consequently, it is difficult to distinguish between the individual contributions of each bond. However, in an acidic environment, although the intensity of the P 2p XPS peak was relatively low, a shift in the binding energy was still observed. After deconvolution, a new peak was obtained at approximately 136.18 eV, which was believed to represent the component of terminal-type P. This type of P is linked only on one side with Al or a small portion of Si after the breakage of the Al-O-P bond in an acidic environment.

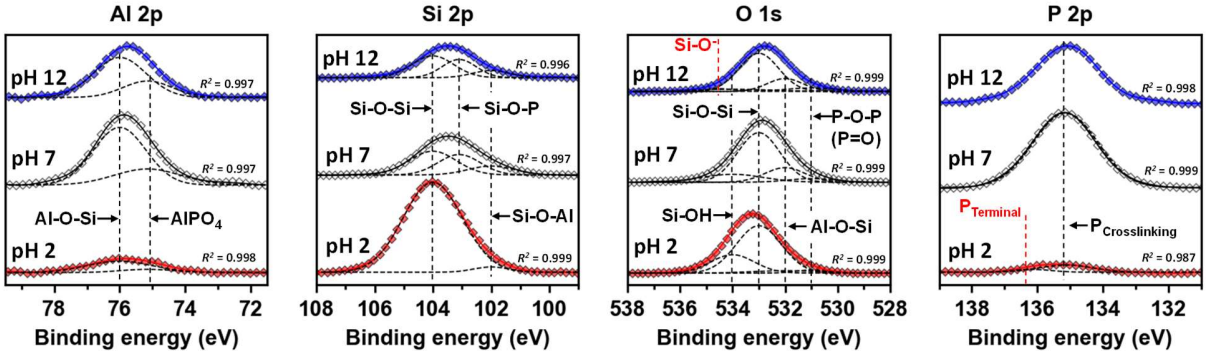

Fig. 11. High-resolution XPS analysis of PGP2 after immersion in pH 2, 7, and 14 solutions.

Table 3. X-ray photoelectron spectroscopy of functional groups of PGP2 sample

Peak name	Functional group	Binging energy (eV)	Proportion (%) pH 2	Proportion (%) pH 7	Proportion (%) pH 12
Al 2p	$AlPO_4$	75.15	18.82	26.26	27.89
	Al-O-Si	76	81.18	73.74	72.11
Si 2p	Si-O-Al	102	5.32	17.16	15.03
	Si-O-P	103.1	-	36.02	34.44
	Si-O-Si	104	94.68	46.82	50.53

O 1s	P-O$^-$ (P=0)	531	2.97	4.98	7.40
	Al-O-Si	532.1	4.68	17.55	19.08
	Si-O-Si	533	67.25	62.76	63.15
	Si-OH	534	25.10	14.71	7.13
	Si-O$^-$	534.5	-	-	3.24
P 2p	Crosslinking-P	135.12	77.54	100	100
	Bridging-P	136.18	22.46	-	-

522

523

524 **3.4. Evaluation of stabilisation/solidification capacity for anions**

525 The leaching of SeO_3^{2-}, SeO_4^{2-}, I^-, and IO_3^- from PGP2 is illustrated in **Fig. 12.** All anions were leached
526 consistently from PGP2-based samples and reached leaching extents of 2.14±0.06%, 3.04±0.12%,
527 3.55±0.05%, and 4.23±0.05% for SeO_3^{2-}, SeO_4^{2-}, I^-, and IO_3^-, respectively, after 28 d.

528

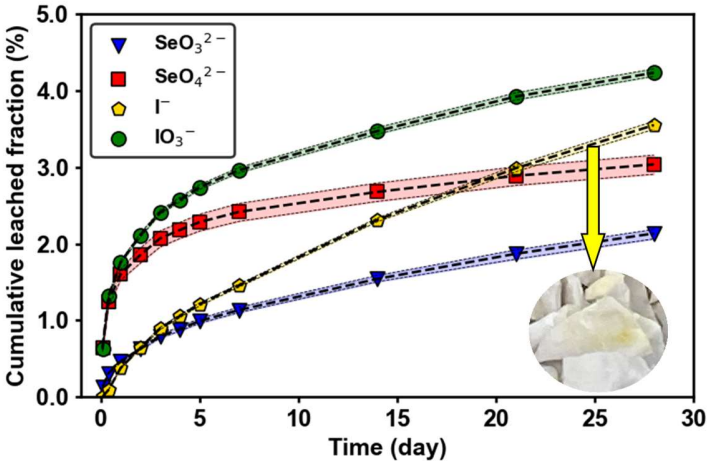

529

530 **Fig. 12.** Cumulative fraction of Se oxyanion (SeO_3^{2-} and SeO_4^{2-}), I^-, and IO_3^- leaching from PGP2 for 28
531 d (confidence intervals are indicated by light-coloured areas).

532

533 **Table 4** shows a comparison of previous studies on the immobilisation of SeO_3^{2-}, SeO_4^{2-}, I^- and IO_3^- onto
534 alkali-activated materials. Tian et al. [36] used Na_2SiO_3 and NaOH as alkali activators to activate
535 geopolymer materials and solidify the Se oxyanions. After an 18-h leaching procedure, it was determined

that the Na_2SiO_3-activated geopolymer exhibited superior efficiency in solidifying SeO_3^{2-} and SeO_4^{2-} compared with NaOH-activated geopolymers, which can be attributed to the variations in the structural compactness of the geopolymer induced by the two different activators. The former results in leaching percentages of 10% and 18%, respectively. In another investigation, the efficacy of alkali-activated geopolymers in immobilising I^- was found to be inadequate, with more than 80% of I^- being leached out over a 21-d leaching period. This outcome was attributed to the weak association between I^- and the geopolymer [67]. In addition, owing to the lack of studies and data on the immobilisation of IO_3^- by alkali-activated geopolymers, the capacities of the typical alkali-absorbent ettringite and layered double hydroxides (LDHs) to immobilise IO_3^- were compared [68, 69]. Although both ettringite and LDHs exhibited some immobilisation capability, the presence of co-mingled SO_4^{2-} and CO_3^{2-} in the vadose zone pore water (VZPW) within cementitious waste forms led to substantial leaching of IO_3^- after the leaching process. To the best of our knowledge, this study shows the highest level of effectiveness among all published reports on the solidification capacity of alkali-activated metakaolin geopolymer substrates for SeO_3^{2-}, SeO_4^{2-}, I^-, and IO_3^-.

Table 4. Leaching of SeO_3^{2-}, SeO_3^{2-}, I^- and IO_3^- from alkaline-activated materials in literature: alkali-activated geopolymer matrices for Se oxyanions and I^-, and other adsorbents for IO_3^-, compared with the PGP in this study.

Condition	SeO_3^{2-}	SeO_4^{2-}	I^-	IO_3^-	reference
S/S in Na_2SiO_3-based GPs	10% (18 h)	18% (18 h)			[36]
S/S in the NaOH-based GPs with calcined hydrotalcite (CHT)	50% (18 h)	60% (18 h)			[36]
S/S in the alkaline-activated metakaolin-based GP			>80% (21 d)		[67]

Iodate substituted ettringite				31% (35 d)	[68]
Iodate doped Mg/Al LDHs				21% (21 d)	[69]
S/S in phosphoric acid-activated metakaolin-based geopolymer	2.14% (28 d)	3.04% (28 d)	3.55% (28 d)	4.23% (28 d)	This study

554

555

556 XRD was employed to study the structural changes occurring during the solidification of anions and
557 leaching of the PGP2 samples. **Figure 13(a)** displays the XRD patterns of the original PGP2 and the
558 PGP2 samples that underwent solidification with anions. The results indicate that the XRD pattern of the
559 PGP2 sample remained unchanged with the anion solidification after the two-stage curing process,
560 displaying the same broad hump in the 2θ range of 15–35° as the original PGP2 sample. The XRD
561 patterns of the PGP2 samples with solidifying anions after 28 d of leaching are shown in **Fig. 13(b)**.
562 After 28 d of leaching, the PGP2 samples with solidified anions maintained the same XRD pattern as
563 previously reported. These results indicate that the crystalline structure of PGP2 did not change after
564 solidifying the anions and could maintain its structural stability, even after 28 d of leaching.

565

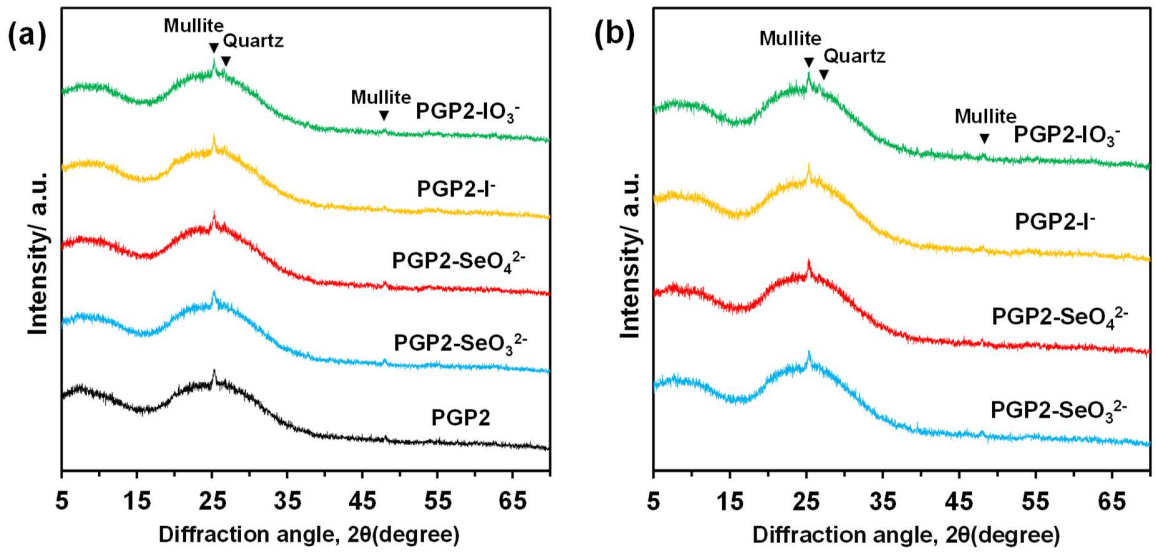

566

Fig. 13. XRD pattern of pure PGP2 and PGP2 samples incorporated with anions of SeO_3^{2-}, SeO_4^{2-}, I^-, and IO_3^- (a) before and (b) after leaching.

The PGP2 samples with the incorporated anions before and after leaching were characterised by FTIR spectroscopy (**Fig. 14**). PGP2 absorption peaks were assigned according to previous studies [38, 70-75]. The absorption peaks located at 1600–1700 cm^{-1} were due to the bending vibration of the OH groups. The peaks at 900–1200 cm^{-1} and 720 cm^{-1} were assigned to the asymmetric and symmetric stretching of Si-O-Si and Al-O-Si, respectively. The peaks at 912, 800, 630, and 450 cm^{-1} were assigned to the stretching and bending vibrations of Si-O-P, Si-O-Si, O-P-O, and Si-O, respectively. Moreover, a faint peak was observed in the CO_3^{2-} vibration mode at 1405 cm^{-1}. This is because the phosphoric acid-activated geopolymers exposed active hydroxyl groups on their surfaces during geopolymerisation (**Fig. 3**), which could easily absorb carbon dioxide from the air and produce carbonation that disappeared after 28 d of leaching. Notably, all the vibration modes of PGP2 remained unaltered after the incorporation of anions (**Fig. 14(a)**). Both intensities and frequencies remained nearly constant, indicating that the PGP2 matrix retained its structural integrity, even after anion incorporation. No new chemical linkages were observed, suggesting a chemical connection between the PGP2 matrix and the anions. Furthermore, consistent FTIR spectra were observed for all PGP2 samples before and after leaching, indicating that PGP2 maintained its structural stability, even after 28 d of leaching (**Fig. 14(b)**).

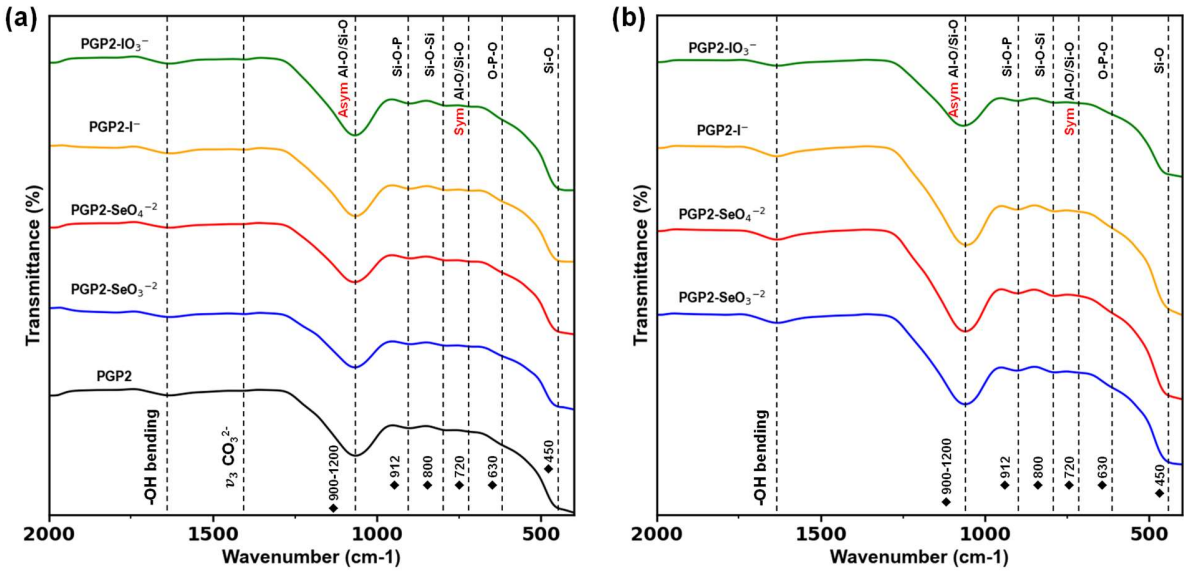

586

587 **Fig. 14.** FTIR spectra of PGP2 samples (a) before and (b) after leaching.

588

589 Based on the leaching results, it is evident that SeO_3^{2-} consistently exhibited a lower leaching rate than I^-
590 and IO_3^-. Conversely, SeO_4^{2-}, which initially demonstrated higher leaching than I^- for up to approximately
591 21 d, experienced a decline in leaching beyond this period, ultimately leaching less than I^- owing to its
592 plateaued leaching curve (**Fig. 12**). Generally, the association of Se and I with the Al or Si tetrahedron is
593 exceedingly challenging due to their distinct structures and charges [76, 77]. Moreover, the FTIR and
594 XRD results demonstrated that the PGP2 matrix did not undergo any structural changes or produce new
595 chemical bonds after the solidification of the anions (**Fig. 13, 14**). Considering the electrostatic
596 interaction as the primary association mode between PGP2 and anions, it is clear that this result is
597 consistent with earlier speculations based on zeta potential (**Fig. 9**). However, the robust solidification
598 capacity of PGP2 for SeO_3^{2-} compared with that for SeO_4^{2-} appeared to contradict the zeta potential
599 results. It is crucial to note that SeO_3^{2-} in PGP is typically present in the form of $HSeO_3^-$ because of its
600 acidic environment [78]. Therefore, despite having a greater electrostatic attraction, its impact on the zeta
601 potential of the PGP surface was not as strong as that of SeO_4^{2-}. Conversely, the PGP sample containing
602 I^- after the 28-d leaching experiment showed a brownish–yellow substance with a distinctly irritating

odour (**Fig. 12**), which was identified as KI. Thus, the high solidification ability of PGP for I^- was also favoured by the precipitation of KI in addition to ionic electrostatic attraction, although I^- had a more pronounced effect on the zeta potential of PGPs than IO_3^- (**Fig. 9**).

4. Conclusions

The surface chemistry and structure-related electrostatic properties of phosphoric-acid-activated MK-based PGPs and their potential in S/S applications were studied and evaluated through zeta potential, microstructure characterisation, immersion behaviour, and leaching experiments. The obtained results provide a theoretical basis for prospective manipulation of the surface electrical characteristics of PGPs. Additionally, the findings provide valuable insights and perspectives on the immobilisation of anionic radionuclides, which can inform the broader integration of PGPs in the domain of nuclear waste management. The following conclusions were drawn:

1) PGPs develop Al_{VI}-OP and Al_{IV}-OP structural units after undergoing geopolymerisation, the ratio of which controls the surface electrostatic properties of the PGPs. Increasing the concentrations of the acid activators led to a higher ratio of these units, resulting in more positively charged sites. An optimal concentration of approximately 10.3 M of the phosphoric acid activator is recommended when activating metakaolin. This concentration effectively supported the geopolymerisation process without inducing excessive dealumination, which could have hindered the reaction.

2) The surfaces of the PGPs demonstrated a zeta potential that initially increased and then decreased as the pH level increased. Typically, the zeta potential reaches its peak value at equilibrium pH in neutral solutions. Within the equilibrium pH range of approximately 2–5, the surfaces of the PGPs carried a positive charge and possessed electrostatic adsorption capabilities for anions such as SeO_3^{2-}, SeO_4^{2-}, I^-, and IO_3^-.

3) When PGPs come into contact with an acidic aqueous environment, their surface structure experiences preferential fracture of the $AlPO_4$ units, which contributes to the dealumination process. This phenomenon became more prominent as the pH decreased, leading to a decreased ratio of Al_{VI}-OP to Al_{IV}-OP and subsequently causing a decline in the positive electrical properties of the PGPs surface. In contrast, PGPs exhibit relatively stable structures in aqueous alkaline environments. However, a large number of Si-OH structural units in the surface structure, along with VI-coordination Al, which exhibits Brønsted acidity in an alkaline environment, lose their protons and generate negative charges. This process intensified with increasing pH, leading to an increase in the negative charge of the PGP surface.

4) The immobilisation of SeO_3^{2-}, SeO_3^{2-}, I^-, and IO_3^- anions within the PGP matrix was highly effective, without any significant changes in the matrix structure observed after the solidification of these anions, even after 28 d of leaching. This effective immobilisation was primarily attributed to the electrostatic attraction between the anions and positively charged structural unit, Al_{VI}-OP, located at the PGP matrix interface. Remarkably, this association led to a significant enhancement in the retention of anions compared with previous studies that utilised different matrices.

CRediT authorship contribution statement

Xiaobo Niu: Conceptualisation, Methodology, Formal analysis, Validation, Writing-original Draft, Investigation, Data Curation, Funding, Writing-review & editing.

Yogarajah Elakneswaran: Conceptualisation, Methodology, Formal analysis, Writing-original Draft, Supervision, Funding, Writing-review & editing.

Naoki Hiroyoshi: Conceptualisation, Methodology, Supervision, Writing-review & editing.

Declaration of Competing Interest

650 The authors declare that they have no known competing financial interests or personal relationships that
651 could have appeared to influence the work reported in this paper.
652
653 **Acknowledgements**
654 JST SPRING, Grant Number JPMJSP2119, and Japan Society for the Promotion of Science (JSPS)
655 Grants-in-Aid for Scientific Research (KAKENHI), Grant No. 21K0420701, supported part of this work.
656 A part of this work was conducted at the Laboratory of XPS analysis, Joint-use facilities, Hokkaido
657 University, supported by "Advanced Research Infrastructure for Materials and Nanotechnology in Japan
658 (ARIM)" of the Ministry of Education, Culture, Sports, Science and Technology (MEXT).
659
660
661
662

References

[1] I. N. Kessides, The future of the nuclear industry reconsidered: Risks, uncertainties, and continued promise, Energy Policy, 48(2012) 185-208. https://doi.org/10.1016/j.enpol.2012.05.008

[2] D. Kaczorowski, J.Ph. Vernot, Wear problems in nuclear industry, Tribol. Int., 39(2006) 1286-1293. https://doi.org/10.1016/j.triboint.2006.02.048

[3] I. G. McKinley, J. M. West, S. M. L. Hardie, A Risk Management Perspective on Climate Change: Lessons Learned from the Nuclear Industry, Environ. Manage., 69(2022) 835–846. https://doi.org/10.1007/s00267-022-01594-y

[4] TEPCO, 2013. Basic Policy for the Contaminated Water Issue at the TEPCO's Fukushima Daiichi Nuclear Power Station. https://www.mofa.go.jp/policy/page3e_000072.html

[5] C. de Boer, I. Catsburg, A Report: The Impact of Nuclear Accidents on Attitudes Toward Nuclear Energy, The Public Opinion Quarterly, 52(1988) 254-261. https://www.jstor.org/stable/2749279

[6] T. Ohba, K. Tanigawa, L. Liutsko, Evacuation after a nuclear accident: Critical reviews of past nuclear accidents and proposal for future planning, Environ. Int., 148(2021) 106379. https://doi.org/10.1016/j.envint.2021.106379

[7] H. Sekimoto, H. Nakamura, N. Takagi, Toxicity of radioactive wastes discharged from nuclear energy centre in the future equilibrium state, Ann. Nucl. Energy, 23(1996), 663-668. https://doi.org/10.1016/0306-4549(95)00031-3

[8] L.A. Kszos, A.J. Stewart, Review of Lithium in the Aquatic Environment: Distribution in the United States, Toxicity and Case Example of Groundwater Contamination, Ecotoxicology, 12(2003), 439–447. https://doi.org/10.1023/A:1026112507664

[9] D. I. Kaplan, M. E. Denham, S. Zhang, C. Yeager, C. Xu, K. A. Schwehr, H. P. Li, Y. F. Ho, D. Wellman, P. H. Santschi, Radioiodine Biogeochemistry and Prevalence in Groundwater, Critical Reviews in Environmental Science and Technology, 44(2013) 2287-2335. https://doi.org/10.1080/10643389.2013.828273

[10] S. Miki, K. Fujimoto, Y. Shigenobu, D. Ambe, H. Kaeriyama, K. Takagi, T. Ono, T. Watanabe, H. Sugisaki, T. Morita, Concentrations of ^{90}Sr and $^{137}Cs/^{90}Sr$ activity ratios in marine fishes after the Fukushima Dai-ichi Nuclear Power Plant accident, Fisheries Oceanography, (26)2017 221-233. https://doi.org/10.1111/fog.12182

[11] G. Jörg, R. Bühnemann, S. Hollas, N. Kivel, K. Kossert, S.V. Winckel, C.L.V. Gostomski, Preparation of radiochemically pure ^{79}Se and highly precise determination of its half-life, Appl. Radiat. Isot., 68 (2010) 2339-2351. https://10.1016/j.apradiso.2010.05.006

[12] Y. Fan, W. Zhou, X. Hou, Pre-nuclear level of ^{129}I in Chinese loess-paleosol sections: A search for the natural ^{129}I level for dating in terrestrial environments, Geochim. Cosmochim. Acta, 231(2018) 64-72. https://doi.org/10.1016/j.gca.2018.04.014

[13] R. Pojasek, Stablilization, solidification of hazardous wastes, Environ. Sci. Technol., 12(1978) 382-386. https://doi.org/10.1021/es60140a607

[14] J. R. Conner, S. L. Hoeffner, The History of Stabilization/Solidification Technology, Environ. Sci. Technol., 28(1998) 325-396. https://doi.org/10.1080/10643389891254241

[15] C. C. Wiles, A review of solidification/stabilisation technology, J. Hazard. Mater., 14(1987) 5-21. https://doi.org/10.1016/0304-3894(87)87002-4

[16] J. Zhang, P. L Bishop, Stabilization/solidification (S/S) of mercury-containing wastes using reactivated carbon and Portland cement, J. Hazard. Mater., 92(2002) 199-212. https://doi.org/10.1016/S0304-3894(02)00019-5

[17] S. A. A. Tajudin, M.A.M. Azmi, A.T.A. Nabila, Stabilization/Solidification Remediation Method for Contaminated Soil: A Review, IOP Conf. Ser.: Mater. Sci. Eng., 136(2016) 27-29. https://doi.org/10.1088/1757-899X/136/1/012043

[18] S.B. Eskander, S.M. Abdel Aziz, H. El-Didamony, M.I. Sayed, Immobilization of low and intermediate level of organic radioactive wastes in cement matrices, J. Hazard. Mater., 190(2011) 969-979. https://doi.org/10.1016/j.jhazmat.2011.04.036

[19] S. Kearney, A. S. Yorkshire, D. A. Geddes, T. Hanein, S. Nelson, J. L. Provis, B. Walkley, Chapter 25 - Cement-based stabilisation/solidification of radioactive waste, Low Carbon Stabilization and Solidification of Hazardous Wastes, 2022 407-431. https://doi.org/10.1016/B978-0-12-824004-5.00005-0

[20] M. I. Ojovan, H. J. Steinmetz, Approaches to Disposal of Nuclear Waste, Energies, 15(2022) 7804. https://doi.org/10.3390/en15207804

[21] P. Duxson, A. Fernández-Jiménez, J. L. Provis, G. C. Lukey, A. Palomo & J. S. J. van Deventer, Geopolymer technology: the current state of the art, J. Mater. Sci., 42(2007) 2917–2933. https://doi.org/10.1007/s10853-006-0637-z

[22] V. Cantarel, T. Motooka, I. Yamagishi, Geopolymers and their potential applications in the nuclear waste management field A bibliographical study (JAEA-Review--2017-014). Japan https://doi.org/10.11484/jaea-review-2017-014

[23] R.S. Krishna, J. Mishra, M. Zribi, F. Adeniyi, S. Saha, S. Baklouti, F. U. A. Shaikh, H.S. Gökçe, A review on developments of environmentally friendly geopolymer technology, Materialia, 20(2021) 101212. https://doi.org/10.1016/j.mtla.2021.101212

[24] J.L. Provis, Geopolymers and other alkali activated materials - Why, how, and what?, Mater. Struct. 47(2014) 11-25. https://doi.org/10.1617/s11527-013-0211-5

730 [25] J. L. Provis and S. A. Bernal, Geopolymers and related alkali-activated materials, Annu. Rev. Mater.
731 Sci., 44(2014) 299-327. https://doi.org/10.1146/annurev-matsci-070813-113515

732 [26] B.I. El-Eswed, R.I. Yousef, M. Alshaaer, I. Hamadneh, S.I. Al-Gharabli, F. Khalili,
733 Stabilization/solidification of heavy metals in kaolin/zeolite based geopolymers, Int. J. Miner. Process.,
734 (137)2015 34-42. https://doi.org/10.1016/j.minpro.2015.03.002

735 [27] TEPCO, n.d. Contaminated Water Treatment. (2023).
736 https://www.tepco.co.jp/en/decommision/planaction/alps/index-e.html

737 [28] S. A. Bernal, J. S. J. van Deventer, J. L. Provis, What happens to 5-year-old metakaolin geopolymers?
738 The effect of alkali cation, Calcined Clays for Sustainable Concrete, (10)2015.
739 https://doi.org/10.1007/978-94-017-9939-3_39

740 [29] A. Palomo, A. Fernández-Jiménez, M. Criado, Geopolymers: same basic chemistry, different
741 microstructures, Mater. Constr., 54(275) (2004), 77–91. https://doi.org/10.3989/mc.2004.v54.i275.249

742 [30] X. Niu, Y. Elakneswaran, R. I. Chaerun, J. L. Provis, T. Sato, Adsorption behaviour of simulant
743 radionuclide cations and anions in metakaolin-based geopolymer, J. Hazard. Mater., 429(2022) 128373.
744 https://doi.org/10.1016/j.jhazmat.2022.128373

745 [31] Q. Tian and K. Sasaki, Application of fly ash-based geopolymer for removal of caesium, strontium
746 and arsenate from aqueous solutions: Kinetic, equilibrium and mechanism analysis. Water Sci. Technol.
747 79(2019) 21162125. https://doi.org/10.2166/wst.2019.209

748 [32] N. Soonthornwiphat, Y. Kobayashi, K. Toda, K. Kuroda, C. R. Islam, T. Otake, Y. Elakneswaran,
749 J. L. Provis, T. Sato, Encapsulation of Sr-loaded titanate spent adsorbents in potassium aluminosilicate
750 geopolymer, J. Nucl. Sci. Technol., 19(2020) 1181-1188.
751 https://doi.org/10.1080/00223131.2020.1775717

752 [33] N. Vandevenne, R. I. Iacobescu, Y. Pontikes, R. Carleer, E. Thijssen, K. Gijbels, S. Schreurs, W.
753 Schroeyers, Incorporating Cs and Sr into blast furnace slag inorganic polymers and their effect on
754 matrices properties. J. Nucl. Mater. 503(2018) 1–12. https://doi.org/10.1016/J.JNUCMAT.2018.02.023

755 [34] Q. Tian, Yi. Bai, Yi. Pan, C. Chen, S. Yao, K. Sasaki, H. Zhang, Application of Geopolymer in
756 Stabilization/Solidification of Hazardous Pollutants: A Review, Molecules, 27(2022) 4570.
757 https://doi.org/10.3390/molecules27144570

758 [35] R. I. Chaerun, N. Soonthornwiphat, K. Toda, K. Kuroda, X. Niu, R. Kikuchi, T. Otake, Y.
759 Elakneswaran, J. L. Provis, T. Sato, Retention Mechanism of Cesium in Chabazite Embedded into
760 Metakaolin-Based Alkali Activated Materials, J. Hazard. Mater., 440(2022) 129732.
761 https://doi.org/10.1016/j.jhazmat.2022.129732.

762 [36] Q. Tian, B. Guo, K. Sasaki, Immobilization mechanism of Se oxyanions in geopolymer: Effects of
763 alkaline activators and calcined hydrotalcite additive, J. Hazard. Mater., 387(2020) 121994,
764 https://doi.org/10.1016/j.jhazmat.2019.121994

765 [37] J. Davidovits, Geopolymer, Chemistry and Applications, (2008).

766 [38] H. Lin, H. Liu, Y. Li, X. Kong, Properties and reaction mechanism of phosphoric acid activated
767 metakaolin geopolymer at varied curing temperatures, Cem. Concr. Res., 144(2021) 106425.
768 https://doi.org/10.1016/j.cemconres.2021.106425

769 [39] M. Fawer, M. Concannon, W. Rieber, Life cycle inventories for the production of sodium silicates,
770 Int. J. Life Cycle Assess., 4(1999) 207-212. https://doi.org/10.1007/BF02979498

771 [40] H.K. Tchakouté, C.H. Rüscher, Mechanical and microstructural properties of metakaolin-based
772 geopolymer cements from sodium waterglass and phosphoric acid solution as hardeners: a comparative
773 study, Appl. Clay Sci., 140(2017) 81-87. https://doi.org/10.1016/j.clay.2017.02.002

774 [41] Y.S. Wang, J.G. Dai, Z. Ding, W.T. Xu, Phosphate-based geopolymer: formation mechanism and
775 thermal stability. Mater. Lett., 190(2017) 209-212. https://doi.org/10.1016/j.matlet.2017.01.022

776 [42] Y.S. Wang, Y. Alrefaei, J.G. Dai, Silico-aluminophosphate and alkali-aluminosilicate geopolymers:
777 a comparative review, Front. Mater., 6(2019) 106. https://doi.org/10.3389/fmats.2019.00106

778 [43] Y. Liu, Y. Meng, X. Qiu, F. Zhou, H. Wang, S. Zhou, C. Yan, Novel porous phosphoric acid-based
779 geopolymer foams for adsorption of Pb(II), Cd(II) and Ni(II) mixtures: Behavior and mechanism, Ceram.
780 Int., 49(2023) 7030-7039. https://doi.org/10.1016/j.ceramint.2022.10.164

781 [44] S. Tome, D. T. Hermann, V. O. Shikuku, S. Otieno, Synthesis, characterisation and application of
782 acid and alkaline activated volcanic ash-based geopolymers for adsorptive remotion of cationic and
783 anionic dyes from water, Ceram. Int., 47(2021) 20965-20973.
784 https://doi.org/10.1016/j.ceramint.2021.04.097

785 [45] S. Pu, Z. Zhu, W. Song, H. Wang, W. Huo, J. Zhang, A novel acidic phosphoric-based geopolymer
786 binder for lead solidification/stabilisation, J. Hazard. Mater., 415(2021) 125659.
787 https://doi.org/10.1016/j.jhazmat.2021.125659

788 [46] H. K. Tchakouté, C. H. Rüscher, E. Kamseu, F. Andreola, C. Leonelli, Influence of the molar
789 concentration of phosphoric acid solution on the properties of metakaolin-phosphate-based geopolymer
790 cements, Appl. Clay Sci., 147(2017) 184-194. https://doi.org/10.1016/j.clay.2017.07.036.

791 [47] F. Taulelle, B. Bouchevreaua, C. Martineaua, NMR crystallography driven structure determination:
792 nanoporous materials, Cryst. Eng. Comm., 15(2013) 8613-8622. https://doi.org/10.1039/C3CE41178H

793 [48] B. Walkley, J.L. Provis, Solid-state nuclear magnetic resonance spectroscopy of cements, Mater.
794 Today Adv., 1(2019) 100007. https://doi.org/10.1016/j.mtadv.2019.100007

795 [49] R. M. Mironenko, O. B. Belskaya, V. P. Talsi, V. A. Likholobov, Quadrupolar magic angle spinning
796 NMR spectra fitted using the Pearson IV function, Solid State Nucl. Magn. Reson., 63–64(2014) 37-41.
797 https://doi.org/10.1016/j.ssnmr.2014.10.001.

798 [50] M. Takeya, A. Ubaidah, M. Shimokawara, H. Okano, T. Nawa, Y. Elakneswaran, Crude
799 oil/brine/rock interface in low salinity waterflooding: Experiments, triple-layer surface complexation
800 model, and DLVO theory, J. Pet. Sci. Eng., 188(2020) 106913.
801 https://doi.org/10.1016/j.petrol.2020.106913.

802 [51] X. Yi, K. Liu, W. Chen, J. Li, S. Xu, C. Li, Y. Xiao, H. Liu, X. Guo, S. Liu, A. Zhen, Origin and
803 Structural Characteristics of Tri-coordinated Extra-framework Aluminum Species in Dealuminated
804 Zeolites, J. Am. Chem. Soc., 140(2018) 10764–10774. https://doi.org/10.1021/jacs.8b04819

805 [52] D. Zhang, D. Wang, Z. Liu, F. Xie, Rheology, agglomerate structure, and particle shape of fresh
806 geopolymer pastes with different NaOH activators content. Constr. Build. Mater., 187(2018) 674–680.
807 https://doi.org/10.1016/j.conbuildmat.2018.07.205.

808 [53] M.-G Barthés-Labrousse, Acid–base characterisation of flat oxide-covered metal surfaces, Vacuum,
809 67(2002) 358-392. https://doi.org/10.1016/S0042-207X(02)00209-9.

810 [54] Y. Yang, J. Tang, H. Song, Y. Yang, Z. Gu, J. Fu, Y. Liu, M. Zhang, Z. Qiao, C. Yu, Dendritic
811 Mesoporous Silica Nanoparticle Adjuvants Modified with Binuclear Aluminum Complex: Coordination
812 Chemistry Dictates Adjuvanticity, Angew. Chem., 59(2020) 19610–19617.
813 https://doi.org/10.1002/anie.202006861

814 [55] E. E. Saka, C. Güler, The effects of electrolyte concentration, ion species and pH on the zeta potential
815 and electrokinetic charge density of montmorillonite, Clay Minerals, 41(2006) 853-861.
816 https://doi.org/10.1180/0009855064140224

817 [56] Y. Kameshima, A. Yasumori, K. Okada, XPS and X-ray AES (XAES) Study of Various Aluminate
818 Compounds, Hyomen Kagaku, 21(2000) 481-487. https://doi.org/10.1380/jsssj.21.481
819 [57] N. Komatsu, T. Satoh, M. Honjo, T. Futatuki, K. Masumoto, C. Kimura, H. Aoki, Influence of
820 inserting AlN between AlSiON and 4H–SiC interface for the MIS structure, Applied Surface Science,
821 257(2011) 8307-8310. https://doi.org/10.1016/j.apsusc.2011.02.107.
822 [58] Ph. Massiot, M.A. Centeno, I. Carrizosa, J.A. Odriozola, Thermal evolution of sol–gel-obtained
823 phosphosilicate solids (SiPO), J. Non. Cryst. Solids, 292(2001) 158-166. https://doi.org/10.1016/S0022-
824 3093(01)00854-7.
825 [59] J. Xiang, R. Zhu, Q. Chen, G. Lv, Y. Yang, A novel montmorillonite-based soil amendment for
826 Cd/REEs immobilisation and nutrients sustained release, Appl. Clay Sci., 221(2022).
827 https://doi.org/10.1016/j.clay.2022.106464.
828 [60] L. Todan, E.M. Anghel, P. Osiceanu, R.V.F. Turcu, I. Atkinson, S. Simon, M. Zaharescu, Structural
829 characterisation of some sol–gel derived phosphosilicate glasses, J. Mol. Struct., 1086(2015) 161-171.
830 https://doi.org/10.1016/j.molstruc.2015.01.012.
831 [61] S. Wang, T. Nguyen, H. Peng, S. Wu, D. Parry, A. Urban, L. Huang, Sodium removal from bauxite
832 desilication product (sodalite) aided by chelating effects of inorganic and organic acids, J. Environ.
833 Manage., 338(2023) 117837. https://doi.org/10.1016/j.jenvman.2023.117837.
834 [62] M. Todea, V. Simon, M. Muresan-Pop, A. Vulpoi, M.M. Rusu, A. Simion, M. Vasilescu, G. Damian,
835 D.M. Petrisor, S. Simon, Silica-based microspheres with aluminum-iron oxide shell for diagnosis and
836 cancer treatment, J. Mol. Struct., 1246(2021) 131149. https://doi.org/10.1016/j.molstruc.2021.131149.
837 [63] Y. Elakneswaran, T. Nawa, K. Kurumisawa, Electrokinetic potential of hydrated cement in relation
838 to adsorption of chlorides, Cem. Concr. Res., 39(2009) 340-344.
839 https://doi.org/10.1016/j.cemconres.2009.01.006.

840 [64] K. Wu, L. Song, Y. Hu, H. Lu, B. K. Kandola, E. Kandare, Synthesis and characterisation of a
841 functional polyhedral oligomeric silsesquioxane and its flame retardancy in epoxy resin, Prog. Org. Coat.,
842 65(2009), 490-497. https://doi.org/10.1016/j.porgcoat.2009.04.008.
843 [65] Ph. Massiot, M. A. Centeno, M. Gouriou, M. I. Domínguez, J. A. Odriozola, Sol–gel obtained
844 silicophosphates as materials to retain caesium at high temperatures, J. Mater. Chem., 13(2003) 67-74.
845 https://doi.org/10.1039/B208698K
846 [66] A. Majjane, A. Chahine, M. Et-tabirou, B. Echchahed, T. Do, P. M. Breen, X-ray photoelectron
847 spectroscopy (XPS) and FTIR studies of vanadium barium phosphate glasses, Mater. Chem. Phys.,
848 143(2014) 779-787. https://doi.org/10.1016/j.matchemphys.2013.10.013.
849 [67] O. Toshihiko, K. Naofumi, T. Kazuya, T. Kohei, U. Satoshi, I. Ryohei, K. Tatsuki, T. Ayaka, K.
850 Daniel, S. Peter, Sorption and solidification of iodide, 21st EGU General Assembly, EGU2019,
851 Proceedings from the conference held 7-12 April 2019 in Vienna, Austria, id.12383.
852 2019EGUGA.2112383O
853 [68] N. M. Avalos, T. Varga, S. T. Mergelsberg, J. A. Silverstein, S. A. Saslow, Behavior of iodate
854 substituted ettringite during aqueous leaching, Applied Geochemistry, 125(2021) 104863.
855 https://doi.org/10.1016/j.apgeochem.2020.104863.
856 [69] F. L. Theiss, G. A. Ayoko, R. L. Frost, Leaching of iodide (I^-) and iodate (IO_3^-) anions from
857 synthetic layered double hydroxide materials, J Colloid Interf Sci., 478(2016) 311-315.
858 https://doi.org/10.1016/j.jcis.2016.06.024.
859 [70] C. A. Rees, J. L. Provis, G. C. Lukey, J. S. J. v. Deventer, In Situ ATR-FTIR Study of the Early
860 Stages of Fly Ash Geopolymer Gel Formation, Langmuir, 23(2007), 9076–9082.
861 https://doi.org/10.1021/la701185g

862 [71] C. A. Rees, J. L. Provis, G. C. Lukey, J. S. J. v. Deventer, Attenuated Total Reflectance Fourier
863 Transform Infrared Analysis of Fly Ash Geopolymer Gel Aging, Langmuir, 23(2007), 8170–8179.
864 https://doi.org/10.1021/la700713g

865 [72] Q. Tian, K. Sasaki, A novel composite of layered double hydroxide/geopolymer for co-
866 immobilisation of Cs^{+} and SeO_4^{2-} from aqueous solution, Sci. Total Environ., 695 (2019), 133799.
867 https://doi.org/10.1016/j.scitotenv.2019.133799

868 [73] W. K. W. Lee and J. S. J. v. Deventer, Use of Infrared Spectroscopy to Study Geopolymerization of
869 Heterogeneous Amorphous Aluminosilicates, Langmuir, 19(2003) 8726–8734.
870 https://doi.org/10.1021/la026127e

871 [74] M. Criado, A. F. Jiménez, A. Palomo, Alkali activation of fly ash: Effect of the SiO_2/Na_2O ratio:
872 Part I: FTIR study, Microporous Mesoporous Mat., 106(2007) 180-191.
873 https://doi.org/10.1016/j.micromeso.2007.02.055

874 [75] W.K.W. Lee, J.S.J. Van Deventer, Effects of anions on the formation of aluminosilicate gel in
875 geopolymers, Ind. Eng. Chem Res., 41 (2002) 4550-4558. https://doi.org/10.1021/ie0109410

876 [76] N. D. Pahlevi, B. Guo, K. Sasaki, Immobilization of selenate in cancrinite using a hydrothermal
877 method, Ceram. Int., (44)2018 8635-8642. https://doi.org/10.1016/j.ceramint.2018.02.083
878 [77] S. Kearney, T. J. Robshaw, J. Turner, C. A. Sharrad, B. Walkley, M. D. Ogden, Encapsulation of
879 iodine-loaded metallated silica materials by a geopolymer matrix, MRS Advances, (7)2022 105–109.
880 https://doi.org/10.1557/s43580-022-00207-4
881 [78] M. Kang, F. Chen, S. Wu, Y. Yang, C. Bruggeman, L. Charlet, Effect of pH on Aqueous Se(IV)
882 Reduction by Pyrite, Environ. Sci. Technol. 45(2011) 2704–2710. https://doi.org/10.1021/es1033553